

Radial basis function ENO and WENO finite difference methods based on the optimization of shape parameters

Jingyang Guo* Jae-Hun Jung[†]

June 23, 2018

Abstract

We present adaptive finite difference ENO/WENO methods by adopting infinitely smooth radial basis functions (RBFs). This is a direct extension of the non-polynomial finite volume ENO/WENO method proposed by authors in [4] to the finite difference ENO/WENO method based on the original smoothness indicator scheme developed by Jiang and Shu [9]. The RBF-ENO/WENO finite difference method slightly perturbs the reconstruction coefficients with RBFs as the reconstruction basis and enhances accuracy in the smooth region by locally optimizing the shape parameters. The RBF-ENO/WENO finite difference methods provide more accurate reconstruction than the regular ENO/WENO reconstruction and provide sharper solution profiles near the jump discontinuity. Furthermore the RBF-ENO/WENO methods are easy to implement in the existing regular ENO/WENO code. The numerical results in 1D and 2D presented in this work show that the proposed RBF-ENO/WENO finite difference method better performs than the regular ENO/WENO method.

keywords Essentially non-oscillatory method, Weighted essentially non-oscillatory method, Radial basis function interpolation, Finite difference method.

1 Introduction

We are interested in solving hyperbolic problems that could contain discontinuous solutions in time. High order numerical approximations of such discontinuous solutions may suffer from the Gibbs phenomenon and the approximations are highly oscillatory, e.g. spectral approximations of discontinuous functions [8]. High order essentially non-oscillatory (ENO) and weighted essentially non-oscillatory (WENO) methods are one of the most powerful methods that solve hyperbolic problems with the Gibbs oscillations much reduced [6, 9, 13]. In [4], we developed non-polynomial ENO and WENO methods based on the non-polynomial reconstruction for the finite volume approximations. The original ENO and WENO methods are based on the polynomial interpolation and its convex combination for the final reconstruction at the cell boundaries [13]. Thus once the number of cells that are participating in the interpolation is fixed, the order of accuracy is also fixed. In [4], we proposed to use non-polynomial bases such as the radial basis functions (RBFs) to improve the fixed order of accuracy of the final reconstruction. The underlying idea is to use non-polynomial functions as the interpolation basis that contain a free parameter. The value of the introduced free parameter is adaptively determined by the local solutions so that the local accuracy is improved and higher order of accuracy than the polynomial order can be achieved. This improvement was made by making the leading error term vanish by the free parameter or at least vanish to a certain order. If the leading error term vanishes, the accuracy is improved particularly when the solution is smooth. In [4], it was shown that the ENO/WENO methods with the non-polynomial basis functions improve the accuracy significantly if the problem is smooth. This paper is a direct extension of our previous work for the finite volume ENO/WENO methods to the finite difference ENO/WENO methods. The formulation of the RBF finite difference ENO/WENO methods is basically same as the finite volume methods, while it is more easier to implement to higher-dimensional problems. In this paper we show that the RBF finite difference ENO/WENO methods work similarly as the RBF finite volume methods and provide supporting numerical examples.

*Department of Mathematics, University at Buffalo, SUNY, Buffalo, NY 14260-2900, USA. (jguo4@buffalo.edu).

[†]Corresponding author. Department of Mathematics, University at Buffalo, SUNY, Buffalo, NY 14260-2900, USA. (jaehun@buffalo.edu).

For the non-polynomial basis, we use the multi-quadric (MQ) RBFs. We note that the hybrid of the RBF method and the WENO method is not new. For example, in [1] a polyharmonic spline was used to solve PDEs on the unstructured grid with the WENO method. The RBF WENO method in [1] took advantages of both the RBF and WENO methods. That is, the hybrid method utilizes the meshless feature of the RBFs, which is beneficial for the unstructured grid. It also took the advantage of the non-oscillatory feature of the WENO method, which efficiently handles discontinuous solutions. However, as the polyharmonic spline was used as the RBF basis, the shape parameter was not free but fixed. In this paper, we are more interested in improving the accuracy rather than the efficiency dealing with the unstructured mesh. In order to improve local accuracy, we adopt infinitely smooth RBFs such as the MQ-RBFs, which contain the free parameter, so-called the shape parameter. By exploiting the shape parameter, we improve the local accuracy. It would be an interesting project to develop a method which utilizes both the meshless feature and the shape parameter of the RBFs with the WENO method on the unstructured grid. We only focus on the accuracy in this paper.

We restrict our discussion to RBFs having only one shape parameter although it would be possible to have multiple shape parameters. One of the advantages of using the shape parameter is that the polynomial interpolation is a limit case of the RBF interpolation. That is, the RBF interpolation becomes equivalent to the polynomial interpolation if the shape parameters vanish [10, 11]. In this paper, we follow the similar procedure in [4] for the finite difference ENO/WENO reconstruction and solve several hyperbolic problems. Since the shape parameters are optimized using all the given information within the given stencil, the method would be oscillatory if the stencil contains discontinuities. To prevent such oscillations, we adopt the monotone polynomial interpolation by measuring the local maxima. To switch back to the regular ENO/WENO method, we only need to have the shape parameter vanish, which makes it easy to implement the RBF-ENO/WENO method in the existing ENO/WENO code.

The paper is composed of the following sections. In Section 2, we briefly explain the RBF interpolation and the optimization of the shape parameter. In Section 3, we explain the regular ENO/WENO finite difference method followed by Section 4 where we compare the polynomial interpolation with the RBF interpolation. The interpolation coefficients for $k = 2$ and $k = 3$ are provided. In Section 5, we provide the numerical examples. For the numerical experiments for discontinuous problems, we first use the monotone polynomial interpolation method for the prevention of oscillations. Then we present the numerical examples for both linear and nonlinear problems and for both scalar and system problems in 1D and 2D. In Section 6, we provide a brief conclusion and our future research.

2 RBF Interpolation and optimization of the shape parameter

We briefly explain the RBF interpolation in one space dimension. Suppose that for a domain $\Omega \subset \mathbb{R}$, a data set $\{(x_i, u_i)\}_{i=1}^N$ is given where the centers $x_i \in \Omega$ are the coordinates and u_i are the function values of the unknown function $u(x)$ at $x = x_i$. The RBF interpolation is given by a linear combination of the radial basis function, $\phi : \Omega \rightarrow \mathbb{R}$. The kernel ϕ at $x = x_i$ is a function of the *radial* distance between x and the center x_i and the shape parameters ε_i , i.e. $\phi = \phi(\|x - x_i\|, \varepsilon_i)$ where $\|x - x_i\|$ is the distance between x and x_i . The Euclidean norm is usually used for $\|x - x_i\|$. Then the RBF interpolation of $u(x)$ based on N data points, $I_N^R u(x)$, is given by

$$I_N^R u(x) = \sum_{i=1}^N \lambda_i \phi(\|x - x_i\|, \varepsilon_i), \quad (1)$$

where λ_i are the expansion coefficients to be determined. Here we note that one can add a low order polynomial term in the right hand side of the above equation to make the interpolation consistent up to a certain degree. In this paper, however, we do not include the low order polynomial term in the RBF interpolation. Using the interpolation condition $I_N^R u(x_i) = u_i, i = 1, \dots, N$, the expansion coefficients are determined by the linear system

$$A \cdot \vec{\lambda} = \vec{u}, \quad (2)$$

where $\vec{\lambda} = [\lambda_1, \dots, \lambda_N]^T$, $\vec{u} = [u_1, \dots, u_N]^T$ and $A_{ij} = \phi(\|x_i - x_j\|, \varepsilon_j)$ is the (ij) element of the interpolation matrix A . If $\phi(r)$ is one of the piecewise smooth RBFs with no shape parameter involved, we will obtain the RBF interpolation explicitly after we solve the linear system. However, if $\phi(r)$ is one of the infinitely smooth RBFs, we still need to determine or pre-assign the value of the shape parameter. One can have shape parameters fixed globally as a constant. Or one can optimize them so that the accuracy of the interpolation is improved. There are various kinds of RBFs [3]. Among those, we use the

multi-quadric (MQ) RBF given by

$$\phi(\|x - x_i\|, \varepsilon_i) = \sqrt{1 + \varepsilon_i^2(x - x_i)^2}. \quad (3)$$

One could use a different form of the MQ-RBF such as $\phi(\|x - x_i\|, \varepsilon_i) = \sqrt{(x - x_i)^2 + \varepsilon_i^2}$, but this form yields a more complicated algebraic expression for the RBF-ENO/WENO formulation than (3).

In [3], it has been discussed that the RBF interpolation may yield spectral convergence. In practice, such a fast convergence depends on several conditions such as the optimization of the shape parameters and the data structure. In this paper, we focus on the optimization of the shape parameter to enhance the overall accuracy. This optimization procedure is the key element of the RBF-ENO/WENO formulation. To explain the optimization procedure below, we first assume that the center set $\{x_i\}$ forms a uniform grid and consider the case of $N = 2$. In the following section, similar analysis will be performed for the RBF-ENO/WENO formulation. It is straightforward to extend the same idea to larger values of N .

Let $x_1 = 0$, $x_2 = \Delta x$ and $\Delta x = x_2 - x_1$ with $N = 2$. Let u_i denote the function value of $u(x)$ at $x = x_i$. For example, $u_{\frac{1}{2}} = u(x_{\frac{1}{2}}) = u(\frac{\Delta x}{2})$. Also we assume that all the shape parameters are variable but same, i.e. $\varepsilon_1 = \varepsilon_2 = \varepsilon$. The value of ε can be either real or complex. Define the error function $E(x) = u(x) - I_N^R(x)$, $x \in [x_1, x_2]$. The interpolation based on the Lagrange polynomials yields the second order convergence in Δx , i.e. $|E(x)| \sim O(\Delta x^2)$. The RBF interpolation, $I_N^R(x)$ is then given by from (1)

$$I_N^R(x) = \lambda_1 \sqrt{1 + \varepsilon^2 x^2} + \lambda_2 \sqrt{1 + \varepsilon^2 (x - \Delta x)^2},$$

where λ_1 and λ_2 are to be computed according to (2).

We evaluate the error function $E(x)$ at $x = x_{\frac{1}{2}}$. With the fixed ε and the obtained λ_1 and λ_2 from (2), the Taylor series of $E(x_{\frac{1}{2}})$ in terms of Δx is given by

$$E(x_{\frac{1}{2}}) = \frac{1}{8} \left(\varepsilon^2 u_{\frac{1}{2}} - u_{\frac{1}{2}}'' \right) \Delta x^2 + O(\Delta x^4), \quad (4)$$

where the superscript $''$ denotes the second derivative in x . The Taylor series of $E(x)$ around $x = x_1$ yields a similar result but the cubic order term appears as below

$$E(x_{\frac{1}{2}}) = \frac{1}{8} (\varepsilon^2 u_1 - u_1'') \Delta x^2 + \frac{1}{16} (\varepsilon^2 u_1' - u_1''') \Delta x^3 + O(\Delta x^4). \quad (5)$$

From (4) and (5), we know that it is possible to obtain the 4th or 3rd order accuracy if we choose the shape parameter ε as

$$\varepsilon^2 = \frac{u_{\frac{1}{2}}''}{u_{\frac{1}{2}}} \text{ for } O(\Delta x^4) \quad \text{or} \quad \varepsilon^2 = \frac{u_1''}{u_1} \text{ for } O(\Delta x^3).$$

Thus the RBF interpolation can achieve higher convergence than the second order expected by the polynomial interpolation. Or at least we know that there exists ε^2 that makes the leading error term vanish and helps the interpolation to achieve higher order accuracy. Note, however, that since u_1 and u_2 are the only given information about the unknown function $u(x)$, the exact value of $u''(x)$ at $x = x_0$ and $x_{\frac{1}{2}}$ and $u(x)$ at $x = x_{\frac{1}{2}}$ are not available. The key idea for the construction of the RBF-ENO/WENO method is that we use the approximation of those values to a certain order based on the function values at the given cells so that we can still obtain the improved order of accuracy. Table 1 shows the adaptation condition of ε that makes the leading error term at $x = x_{\frac{1}{2}}$ vanish when expanded in the Taylor series around $x = x_{\frac{1}{2}}$ for different values of N with centers $x_i = (i - 1)\Delta x$, $i = 1, \dots, N$. The table shows the leading interpolation errors with different N when the interpolation is obtained as the polynomials ($\varepsilon = 0$, *Polynomial order*) and RBFs when the adaptation is applied (*RBF order*). As shown in the table the error of the RBF interpolation is of $O(\Delta x^{N+2})$ for $N = 2$ because of the symmetry and of $O(\Delta x^{N+1})$ for the rest while the error of the polynomial interpolation is of $O(\Delta x^N)$ for every N .

3 1D Finite difference ENO/WENO method

Given a uniform grid with N number of points

$$a = x_{\frac{1}{2}} < x_{\frac{3}{2}} < \dots < x_{N-\frac{1}{2}} < x_{N+\frac{1}{2}} = b,$$

Table 1: Adaptation conditions of ϵ for various values of N .

N	Adaptation condition for ϵ	Polynomial order	RBF order
2	$\epsilon^2 h_{\frac{1}{2}} - h_{\frac{1}{2}}'' = 0$	$O(\Delta x^2)$	$O(\Delta x^4)$
3	$3\epsilon^2 h_{\frac{1}{2}}' + h_{\frac{1}{2}}''' = 0$	$O(\Delta x^3)$	$O(\Delta x^4)$
4	$9\epsilon^4 h_{\frac{1}{2}} - 12\epsilon^2 h_{\frac{1}{2}}'' - h_{\frac{1}{2}}^{(4)} = 0$	$O(\Delta x^4)$	$O(\Delta x^5)$
5	$75\epsilon^4 h_{\frac{1}{2}}' + 40\epsilon^2 h_{\frac{1}{2}}''' + h_{\frac{1}{2}}^{(5)} = 0$	$O(\Delta x^5)$	$O(\Delta x^6)$

for the i -th cell $I_i = [x_{i-\frac{1}{2}}, x_{i+\frac{1}{2}}]$, define the cell center x_i and uniform grid spacing Δx as

$$x_i = \frac{1}{2}(x_{i-\frac{1}{2}} + x_{i+\frac{1}{2}}), \quad \Delta x = x_{i+\frac{1}{2}} - x_{i-\frac{1}{2}}, \quad i = 1, 2, \dots, N.$$

The semi-discretized form of the 1D hyperbolic equation

$$u_t(x, t) + f_x(u(x, t)) = 0$$

is a system of ordinary differential equations

$$\left. \frac{du_i(t)}{dt} = - \frac{\partial f(u(x, t))}{\partial x} \right|_{x=x_i} \quad (6)$$

where $u_i(t)$ is a numerical approximation to $u(x_i, t)$ and f is the flux function. While the finite volume method reconstructs the cell boundary values of the solution, the finite difference method seeks the reconstruction of the flux function at the cell boundaries. Define the numerical flux function $h(x, t)$ for each cell

$$f(u(x, t)) = \frac{1}{\Delta x} \int_{x-\frac{\Delta x}{2}}^{x+\frac{\Delta x}{2}} h(\xi, t) d\xi.$$

Differentiate both sides and evaluate them at $x = x_i$ to obtain

$$\left. \frac{\partial f(u(x, t))}{\partial x} \right|_{x=x_i} = \frac{1}{\Delta x} [h(x_{i+\frac{1}{2}}, t) - h(x_{i-\frac{1}{2}}, t)].$$

Therefore, (6) becomes

$$\frac{du_i(t)}{dt} = - \frac{1}{\Delta x} [h_{i+\frac{1}{2}} - h_{i-\frac{1}{2}}], \quad (7)$$

where $h_{i\pm\frac{1}{2}} = h(x_{i\pm\frac{1}{2}}, t)$. Given grid values of f , $f_i = f(u(x_i, t)) = \frac{1}{\Delta x} \int_{x_{i-\frac{1}{2}}}^{x_{i+\frac{1}{2}}} h(\xi, t) d\xi$, the high order reconstruction of $\hat{f}_{i\pm\frac{1}{2}} = h_{i\pm\frac{1}{2}} + O(\Delta x^m)$ needs to be computed, where m depends on the number of cells we use.

For the k -th order ENO reconstruction, we choose the stencil based on r cells to the left and s cells to the right including I_i such that

$$r + s + 1 = k.$$

Define $S_r(i)$ as the stencil composed of those k cells including the cell I_i

$$S_r(i) = \{I_{i-r}, \dots, I_{i+s}\}, \quad r = 0, \dots, k-1. \quad (8)$$

Define a primitive function $H(x)$ such that

$$H(x) = \int_{x_{i-r-\frac{1}{2}}}^x h(\xi) d\xi \quad (9)$$

where the lower limit in the integral can be any cell boundary [12]. By the definition of $H(x)$ in (9), it is obvious that $H'(x) = h(x)$. Then for $i - r - 1 \leq l \leq i + s$, $H(x_{l+\frac{1}{2}})$ is given by the linear sum of cell averages

$$H(x_{l+\frac{1}{2}}) = \sum_{j=i-r}^l \int_{x_{j-\frac{1}{2}}}^{x_{j+\frac{1}{2}}} h(\xi) d\xi = \sum_{j=i-r}^l \Delta x f_j.$$

The regular ENO method constructs the polynomial interpolation of $H(x)$ based on $H(x_{l+\frac{1}{2}})$, $i - r - 1 \leq l \leq i + s$, while the RBF-ENO method constructs the RBF interpolation of $H(x)$. Suppose $P(x)$ is some interpolation for $H(x)$ such that

$$P(x) = H(x) + O(\Delta x^{k+1}). \quad (10)$$

Then $p(x) \equiv P'(x)$ is the function we seek to approximate $h(x)$ where

$$p(x) = h(x) + O(\Delta x^k). \quad (11)$$

Then the numerical flux function is given by the linear combination of the given flux value at each point

$$\hat{f}_{i+\frac{1}{2}}^{(r)} \equiv p(x_{i+\frac{1}{2}}) = \sum_{j=0}^{k-1} c_{rj} f_{i-r+j}$$

where c_{rj} are fixed constants for the ENO method but are variables for the RBF-ENO method.

The WENO method seeks the reconstruction as a convex combination of all possible ENO reconstructions. Suppose the stencil (8) produces k different reconstructions to the value $\hat{f}_{i+\frac{1}{2}}^{(r)}$. Then the WENO reconstruction would take the convex combination of all $\hat{f}_{i+\frac{1}{2}}^{(r)}$:

$$\hat{f}_{i+\frac{1}{2}} = \sum_{r=0}^{k-1} w_r \hat{f}_{i+\frac{1}{2}}^{(r)}, \quad (12)$$

where

$$w_r = \frac{\alpha_r}{\sum_{s=0}^{k-1} \alpha_s}, \quad r = 0, \dots, k-1$$

with

$$\alpha_r = \frac{d_r}{(\epsilon_M + \beta_r)^2}.$$

Here d_r are the polynomial expansion coefficients and $\epsilon_M > 0$ is introduced to avoid the case that the denominator becomes zero usually taken as $\epsilon_M = 10^{-6}$. β_r are the ‘‘smoothness indicators’’ of the stencil $S_r(i)$. In this work, we use the smoothness indicators developed in [9]. The usage of different smoothness indicators found in other WENO variations such as the WENO-Z method [2], WENO-M method [7] or WENO-P method [5] will be considered in our future work.

4 1D reconstruction based on RBFs

The 1D and 2D finite difference RBF-ENO method is a direct extension of the finite volume RBF-ENO method [4]. We only replace the cell averages \bar{u}_i with the nodal flux function f_i . First we consider the case of $k = 2$, that is, two cells are used for the reconstruction. For this case, three flux values, f_{i-1} , f_i and f_{i+1} are available. To reconstruct the boundary values of $f_{i+\frac{1}{2}}$ and $f_{i-\frac{1}{2}}$, we use either $\{f_{i-1}, f_i\}$ or $\{f_i, f_{i+1}\}$. Which flux values should be used is decided by the Newton’s divided difference method [12]. Assume that we decided to use $\{f_i, f_{i+1}\}$ from the Newton’s divided difference. We only show the reconstruction at cell boundary $x = x_{i+\frac{1}{2}}$. The reconstruction at $x = x_{i-\frac{1}{2}}$ can be achieved in the same manner. Based on the definition of $H(x)$ in (9) we have

$$H(x_{i-\frac{1}{2}}) = -\Delta x \cdot f_i, \quad H(x_{i+\frac{1}{2}}) = 0, \quad H(x_{i+\frac{3}{2}}) = \Delta x \cdot f_{i+1}.$$

4.1 Polynomial interpolation for regular ENO

The polynomial interpolation $P(x)$ is given as

$$P(x) = \lambda_1 + \lambda_2 x + \lambda_3 x^2.$$

Let $\vec{H} = [H_{i-\frac{1}{2}}, H_{i+\frac{1}{2}}, H_{i+\frac{3}{2}}]^T$, $\vec{\lambda} = [\lambda_1, \lambda_2, \lambda_3]^T$ and the interpolation matrix A be

$$A = \begin{bmatrix} 1 & x_{i-\frac{1}{2}} & x_{i-\frac{1}{2}}^2 \\ 1 & x_{i+\frac{1}{2}} & x_{i+\frac{1}{2}}^2 \\ 1 & x_{i+\frac{3}{2}} & x_{i+\frac{3}{2}}^2 \end{bmatrix}.$$

Then the expansion coefficients λ_i are given by solving the linear system $\vec{H} = A \cdot \vec{\lambda}$. After taking the first derivative of $P(x)$ and plugging it in $x = x_{i+\frac{1}{2}}$, we obtain the numerical flux function $\hat{f}_{i+\frac{1}{2}}$

$$\hat{f}_{i+\frac{1}{2}} \equiv p(x_{i+\frac{1}{2}}) = \frac{1}{2} \cdot f_i + \frac{1}{2} \cdot f_{i+1}. \quad (13)$$

Expanding $\hat{f}_{i+\frac{1}{2}}$ around $x = x_{i+\frac{1}{2}}$ in the Taylor series yields

$$\hat{f}_{i+\frac{1}{2}} \equiv p(x_{i+\frac{1}{2}}) = h_{i+\frac{1}{2}} + \frac{1}{6} h''_{i+\frac{1}{2}} \Delta x^2 + \frac{1}{120} h^{(4)}_{i+\frac{1}{2}} \Delta x^4 + O(\Delta x^6). \quad (14)$$

The first term in the right hand side of (14) is the exact value of $h(x)$ at $x = x_{i+\frac{1}{2}}$. Thus we confirm that (13) is a 2nd order reconstruction of f .

4.2 Multi-Quadratic RBF interpolation

Now we consider the RBF reconstruction of f . The MQ-RBF interpolation $P(x)$ for $H(x)$ is given as

$$P(x) = \lambda_1 \sqrt{1 + \epsilon^2(x - x_{i-\frac{1}{2}})^2} + \lambda_2 \sqrt{1 + \epsilon^2(x - x_{i+\frac{1}{2}})^2} + \lambda_3 \sqrt{1 + \epsilon^2(x - x_{i+\frac{3}{2}})^2}.$$

Accordingly the interpolation matrix A is given by

$$A = \begin{bmatrix} 1 & \sqrt{\Delta x^2 \epsilon^2 + 1} & \sqrt{4\Delta x^2 \epsilon^2 + 1} \\ \frac{1}{\sqrt{\Delta x^2 \epsilon^2 + 1}} & 1 & \frac{1}{\sqrt{\Delta x^2 \epsilon^2 + 1}} \\ \frac{1}{\sqrt{4\Delta x^2 \epsilon^2 + 1}} & \frac{1}{\sqrt{\Delta x^2 \epsilon^2 + 1}} & 1 \end{bmatrix}.$$

We take the first derivative of $P(x)$ to obtain the numerical flux at $x_{i+\frac{1}{2}}$

$$\hat{f}_{i+\frac{1}{2}} = \left(\frac{\sqrt{4\epsilon^2 \Delta x^2 + 1} + 1}{4\sqrt{\epsilon^2 \Delta x^2 + 1}} \right) \cdot f_i + \left(\frac{\sqrt{4\epsilon^2 \Delta x^2 + 1} - 1}{4\sqrt{\epsilon^2 \Delta x^2 + 1}} \right) \cdot f_{i+1}. \quad (15)$$

Expanding $\hat{f}_{i+\frac{1}{2}}$ around $x = x_{i+\frac{1}{2}}$ in the Taylor series yields

$$\begin{aligned} \hat{f}_{i+\frac{1}{2}} &= h_{i+\frac{1}{2}} + \left(\frac{1}{2} \epsilon^2 h_{i+\frac{1}{2}} + \frac{1}{6} h''_{i+\frac{1}{2}} \right) \Delta x^2 \\ &\quad + \left(-\frac{9}{8} \epsilon^4 h_{i+\frac{1}{2}} + \frac{1}{12} \epsilon^2 h''_{i+\frac{1}{2}} + \frac{1}{120} h^{(4)}_{i+\frac{1}{2}} \right) \Delta x^4 + O(\Delta x^6). \end{aligned} \quad (16)$$

Thus we observe that (15) is at least 2nd order accurate to $h_{i+\frac{1}{2}}$. If we take the value of ϵ as below

$$\epsilon^2 = -\frac{1}{3} \frac{h''_{i+\frac{1}{2}}}{h_{i+\frac{1}{2}}}, \quad (17)$$

then the 2nd order error term vanishes and we obtain a 4th order accurate approximation. We notice that the coefficients of f_i and f_{i+1} in (15) have complicated forms involving a calculation of square roots. This is common among infinitely smooth RBF interpolations because of the existence of undetermined shape parameters. If we fix the shape parameter ϵ as a constant, the reconstruction would have simpler

forms as the piecewise smooth RBF interpolation, but lose the ability to improve accuracy. In order to simplify the form, we expand the right hand side of (15) as below

$$\begin{aligned} \hat{f}_{i+\frac{1}{2}} &= \left(\frac{1}{2} + \frac{1}{4}\epsilon^2\Delta x^2 - \frac{9}{16}\epsilon^4\Delta x^4 \right) \cdot f_i + \left(\frac{1}{2} + \frac{1}{4}\epsilon^2\Delta x^2 - \frac{9}{16}\epsilon^4\Delta x^4 \right) \cdot f_{i+1} \\ &\quad + O(\Delta x^6). \end{aligned} \quad (18)$$

Ignoring all the high order terms in (18) yields

$$\hat{f}_{i+\frac{1}{2}} = \left(\frac{1}{2} + \frac{1}{4}\epsilon^2\Delta x^2 \right) \cdot f_i + \left(\frac{1}{2} + \frac{1}{4}\epsilon^2\Delta x^2 \right) \cdot f_{i+1}. \quad (19)$$

Expanding f_i and f_{i+1} in terms of $h(x)$ we get

$$\begin{aligned} \hat{f}_{i+\frac{1}{2}} &= h_{i+\frac{1}{2}} + \left(\frac{1}{2}\epsilon^2 h_{i+\frac{1}{2}}'' + \frac{1}{6} h_{i+\frac{1}{2}}'''' \right) \Delta x^2 \\ &\quad + \left(\frac{1}{12}\epsilon^2 h_{i+\frac{1}{2}}'''' + \frac{1}{120} h_{i+\frac{1}{2}}^{(4)} \right) \Delta x^4 + O(\Delta x^6). \end{aligned} \quad (20)$$

Thus (19) yields the same 4th order accuracy equivalently to (15) when (17) is used.

Now we consider the evaluation of ϵ in (17) to achieve higher order accuracy than the 2nd order. To explain this, we use the reconstruction at $x = x_{i+\frac{1}{2}}$ as an example. The case of $x = x_{i-\frac{1}{2}}$ can be done in the same manner. The idea is that although the ENO method chooses either $\{f_i, f_{i+1}\}$ or $\{f_i, f_{i-1}\}$ for the final reconstruction, all three flux function values are available when the Newton's divided difference method is applied. Thus we calculate $h_{i+\frac{1}{2}}$ and $h_{i+\frac{1}{2}}''$ based on f_{i-1}, f_i and f_{i+1} . Construct the Lagrange interpolation of $H(x)$ based on $H_{i-\frac{3}{2}}, H_{i-\frac{1}{2}}, H_{i+\frac{1}{2}}, H_{i+\frac{3}{2}}$ and take the first derivative of $H(x)$ at $x = x_{i+\frac{1}{2}}$. Then we have

$$h_{i+\frac{1}{2}} \approx -\frac{1}{6}f_{i-1} + \frac{5}{6}f_i + \frac{1}{3}f_{i+1} + O(\Delta x^3).$$

The second derivative of $h_{i+\frac{1}{2}}$ is approximated by the third derivative of $H(x)$, which is given by

$$h_{i+\frac{1}{2}}'' \approx \frac{f_{i-1} - 2f_i + f_{i+1}}{\Delta x^2} + O(\Delta x).$$

Then by plugging the above approximations of $h_{i+\frac{1}{2}}$ and $h_{i+\frac{1}{2}}''$ into (17), we approximate the optimal value of ϵ^2 as below

$$\epsilon^2 \approx \frac{2}{\Delta x^2} \cdot \frac{-f_{i-1} + 2f_i - f_{i+1}}{-f_{i-1} + 5f_i + 2f_{i+1}}. \quad (21)$$

Note that ϵ can be a complex number because ϵ^2 can be a negative real number. Since ϵ^2 is used instead of ϵ , the final reconstruction is still done with the real operation. If we replace ϵ^2 in (16) with that in (21), we get the following

$$\hat{f}_{i+\frac{1}{2}} \equiv p(x_{i+\frac{1}{2}}) = h_{i+\frac{1}{2}} + \frac{1}{12} h_{i+\frac{1}{2}}^{(3)} \Delta x^3 + O(\Delta x^4).$$

Thus if ϵ^2 is chosen as in (21), the reconstruction (19) still yields a 3rd order accuracy although we do not completely make the 2nd order term in (20) vanish.

4.3 Reconstruction coefficients

Tables 2 and 3 show the reconstruction coefficients for $k = 2$ and $k = 3$, respectively for the MQ RBF-ENO reconstruction. These are the same as for the finite volume method provided in [4]. The difference is that the flux function is used for the calculation of the optimal value of ϵ^2 , while the cell average of the solution is used for the finite volume method. As we see in these tables, the RBF-ENO reconstruction is a perturbed reconstruction of the polynomial-based ENO interpolation. We also observe that the coefficients for $k = 2$ are not consistent while those for $k = 3$ are consistent. Here note that when the shape parameter vanishes, i.e. when $\epsilon \rightarrow 0$, the MQ-RBF reconstruction is reduced into the polynomial reconstruction. For this equivalence known as the polynomial limit [10, 11], one can easily switch the RBF-ENO to the regular ENO and it is easy to convert the existing ENO code into the RBF-ENO code.

Table 4 shows the leading error terms we want to make vanish as in (16) to achieve (k+1)th order of convergence when k cells are used. The adaptation condition becomes complicated for the approximation of ϵ when the value of k becomes large. We leave efficient evaluation methods of ϵ for larger values of k for our future work.

Table 2: Left: The polynomial reconstruction coefficients. Right: The MQ-RBF reconstruction coefficients c_{rj} in (19). $\eta = \epsilon^2 \Delta x^2$.

k	r	j=0	j=1
2	-1	$\frac{3}{2}$	$-\frac{1}{2}$
	0	$\frac{1}{2}$	$\frac{1}{2}$
	1	$-\frac{1}{2}$	$\frac{3}{2}$
$\eta = 0$			

k	r	j=0	j=1
2	-1	$\frac{3}{2} - \frac{3}{2}\eta$	$-\frac{1}{2} + \frac{1}{2}\eta$
	0	$\frac{1}{2} + \frac{1}{4}\eta$	$\frac{1}{2} + \frac{1}{4}\eta$
	1	$-\frac{1}{2} + \frac{1}{2}\eta$	$\frac{3}{2} - \frac{3}{2}\eta$
$\eta = \epsilon^2 \Delta x^2 = \frac{2(-f_{i-1} + 2f_i - f_{i+1})}{-f_{i-1} + 5f_i + 2f_{i+1}}$			

Table 3: Left: The polynomial reconstruction. Right: The MQ-RBF reconstruction coefficients c_{rj} , $\eta = \epsilon^2 \Delta x^2$.

k	r	j=0	j=1	j=2
3	-1	$\frac{6}{11}$	$-\frac{7}{6}$	$\frac{1}{3}$
	0	$\frac{1}{3}$	$\frac{5}{6}$	$-\frac{1}{6}$
	1	$-\frac{1}{6}$	$\frac{5}{6}$	$\frac{1}{3}$
	2	$\frac{1}{3}$	$-\frac{7}{6}$	$\frac{11}{6}$
$\eta = 0$				

k	r	j=0	j=1	j=2
3	-1	$\frac{6}{11} - \frac{9}{2}\eta$	$-\frac{7}{6} + 6\eta$	$\frac{1}{3} - \frac{3}{2}\eta$
	0	$\frac{1}{3} + \frac{5}{6}\eta$	$\frac{5}{6} - \frac{2}{3}\eta$	$-\frac{1}{6} - \frac{1}{6}\eta$
	1	$-\frac{1}{6} - \frac{1}{6}\eta$	$\frac{5}{6} - \frac{2}{3}\eta$	$\frac{1}{3} + \frac{5}{6}\eta$
	2	$\frac{1}{3} - \frac{3}{2}\eta$	$-\frac{7}{6} + 6\eta$	$\frac{11}{6} - \frac{9}{2}\eta$
$\eta = \epsilon^2 \Delta x^2 = \frac{f_{i-1} - 3f_i + 3f_{i+1} - f_{i+2}}{f_{i-1} - 15f_i + 15f_{i+1} - f_{i+2}}$				

5 Numerical experiments

For the numerical example, we compare the developed method with the original ENO/WENO method denoted by the ENO/WENO-JS developed by Jiang and Shu [9]. For the WENO method we use the smoothness indicators developed in [9] and denote our proposed RBF-WENO method as the RBF-WENO-JS method. One can adopt other developments rather than the original WENO method for the RBF-WENO method such as the WENO-Z method [2], which will be investigated in our future research. For the numerical experiments, we use the Lax-Friedrich flux scheme with the 3rd order TVD Runge-Kutta method [14] for the time integration.

5.1 Polynomial limit and non-oscillatory reconstruction

The ENO method uses adaptive stencil to avoid the reconstruction across the possible discontinuity. The RBF-ENO method, however, as the WENO reconstruction, utilizes all available flux functions to optimize the shape parameter within the stencil $S_r(i)$. Thus the final reconstruction can be oscillatory. To prevent the oscillation and recover the ENO property, one can easily switch the RBF-ENO reconstruction to the ENO reconstruction by using the polynomial limit of RBFs. That is, if the shape parameter ϵ vanishes, the RBF reconstruction becomes equivalent to the polynomial reconstruction and becomes the regular ENO reconstruction. In [4] the monotone polynomial method was proposed to use the polynomial limit whenever it is necessary. For the finite difference RBF-ENO method, we follow the same procedure. The difference is that for the local extrema we use the flux function f_i given at each x_i instead of the solution u_i .

The optimized value of ϵ^2 in (17) involves the second derivative of h , e.g. $h''_{i+\frac{1}{2}}$. For $k = 2$, there are three cells involved and only one h'' is to be computed while for $k = 3$, three possible values of h'' are to be computed. For the illustration consider the case of $k = 2$. For $k = 3$, the same procedure is straightforwardly applied for each ENO block. For $k = 2$, the whole interval of x in the stencil is $x_{i-\frac{3}{2}} \leq x \leq x_{i+\frac{3}{2}}$. Without loss of generality, let $x_{i-\frac{3}{2}} = 0$ and $x_{i+\frac{3}{2}} = 3\Delta x$. In this interval, $h(x)$ is

Table 4: Adaptation conditions of ϵ for various values of k . $h_j = h(x_{i+\frac{1}{2}})$ or $h(x_{i-\frac{1}{2}})$.

k	coefficient in the leading error term $O(\Delta x^k)$
2	$\epsilon^2 h_j + \frac{1}{3} h_j'' = 0$
3	$\epsilon^2 h_j' + \frac{1}{12} h_j''' = 0$
4	$15\epsilon^4 h_j + 8\epsilon^2 h_j'' + \frac{1}{5} h_j^{(4)} = 0$
5	$1275\epsilon^4 h_j' + 185\epsilon^2 h_j''' + \frac{7}{3} h_j^{(5)} = 0$

approximated by the second order polynomial and its local extrema exists at $x = x_p$

$$x_p = \frac{-2f_{i-1} + 3f_i - f_{i+1}}{-f_{i-1} + 2f_i - f_{i+1}} \Delta x. \quad (22)$$

If x_p exists inside the given stencil, $p(x)$ is not a monotone function. We use the polynomial limit if x_p exists inside the interval of $S_r(i)$. Thus the polynomial limit condition is given by

$$\epsilon^2 = \begin{cases} 0 & \text{if } 0 < \frac{-2f_{i-1} + 3f_i - f_{i+1}}{-f_{i-1} + 2f_i - f_{i+1}} < 3 \\ -\frac{1}{3} \frac{h_{i+\frac{1}{2}}''}{h_{i+\frac{1}{2}}} & \text{otherwise} \end{cases}. \quad (23)$$

5.2 1D Numerical examples

5.2.1 Advection equation I: smooth initial condition

First we consider the linear scalar equation in $x \in [-1, 1]$

$$u_t + u_x = 0, \quad t > 0, \quad (24)$$

with the initial condition

$$u(x, 0) = u_0(x) = \sin(\pi x) \quad (25)$$

and the periodic boundary condition. The CFL condition is given by $\Delta t \leq C\Delta x$ with $C = 0.1$. Tables 5 and 6 show the L_1, L_2 and L_∞ errors for each method at the final time $T = 0.5$ with $k = 2$ and $k = 3$, respectively. As shown in the tables, for $k = 2$, the RBF-ENO method has almost 3rd order convergence while the regular ENO method yields 2nd order of accuracy or less. The RBF-ENO is also better performed than the WENO-JS in terms of accuracy while the rates of convergence are similar. The RBF-WENO-JS with $k = 2$ is also better than WENO-JS both in accuracy and convergence. We have similar results for $k = 3$. For $k = 3$ the RBF-ENO method yields convergence higher than 3rd order and the RBF-WENO-JS method higher than 5th order while the regular ENO method is about 3rd order and the WENO-JS is about 5th order accurate.

5.2.2 Advection equation II: non-smooth initial condition

We consider the same advection equation (24) but with the discontinuous initial condition

$$u(x, 0) = -\text{sgn}(x), \quad (26)$$

and the boundary condition $u(-1, t) = 1, t > 0$. Here $\text{sgn}(x)$ is the sign function of x . Figure 1 shows solutions at $T = 0.5$ by each method with $N = 200$. The top two figures show the solutions with $k = 2$ and the bottom two figures with $k = 3$. As shown in the figures, the Gibbs oscillations are not significant and the RBF-ENO and RBF-WENO-JS methods yield almost non-oscillatory solutions. For $k = 2$, the RBF-ENO and RBF-WENO-JS solutions are similar and have sharper solution profiles than the regular ENO and WENO methods. For $k = 3$. The RBF-WENO-JS solution is slightly sharper than the WENO-JS solution. The RBF-ENO solution is sharper than the ENO solution but smoother than the RBF-WENO-JS or WENO-JS solutions.

5.2.3 Burger's equation

We consider the Burgers' equation for $x \in [-1, 1]$

$$u_t + \left(\frac{1}{2}u^2\right)_x = 0, \quad t > 0, \quad (27)$$

with the initial condition

$$u(x, 0) = -\sin(\pi x). \quad (28)$$

Tables 7 and 8 show various errors for each case for $k = 2$ and $k = 3$, respectively. For $k = 2$, the RBF-ENO and RBF-WENO-JS methods yield much better accuracy than the ENO or WENO-JS methods, e.g. L_∞ errors. For $k = 3$, the RBF-WENO-JS method yields convergence higher than 5th order while the WENO-JS is about 5th order accurate. The RBF-ENO solution yields convergence higher than 3rd order while the regular ENO solution is about 3rd order or less accurate.

Figure 2 shows the solution profiles at the final time $T = \frac{1}{\pi}$ when the shock forms with $k = 2$ and $k = 3$. The top figures show the solutions for $k = 2$ and the bottom for $k = 3$. For both cases, the RBF-WENO-JS and WENO-JS show similar results while the RBF-ENO solution is better than the regular ENO solution.

5.2.4 Euler equation I: Sod problem

For the system problem, we consider the one-dimensional Euler equations for gas dynamics

$$U_t + F(U)_x = 0, \quad (29)$$

where the conservative state vector U and the flux function F are given by

$$U = (\rho, \rho u, E)^T, \quad F(U) = (\rho u, \rho u^2 + P, (E + P)u)^T.$$

Here ρ, u, P and E denote density, velocity, pressure and total energy, respectively. The equation of state is given by

$$P = (\gamma - 1) \left(E - \frac{1}{2} \rho u^2 \right),$$

where $\gamma = 1.4$ for the ideal gas. We consider the Sod shock tube problem with the initial condition

$$(\rho, u, P) = \begin{cases} (1, 0, 1) & x \leq 0 \\ (0.125, 0, 0.1) & x > 0 \end{cases}.$$

The Sod problem is solved with $N = 200$ and the CFL number $C = 0.1$. Figures 3 and 4 show solutions by each method at the final time $T = 0.2$ for $k = 2$ and $k = 3$, respectively. The top left figure shows the global solution in the entire domain while the rest shows the solution profiles in the areas specified in the top left figure. As in the previous examples, for $k = 2$ the RBF-ENO and RBF-WENO-JS methods are better performed than the regular ENO and WENO-JS methods. The solution profiles are much sharper near the non-smooth area. For $k = 3$, the RBF-WENO-JS solution is similar to the WENO-JS solution while the RBF-ENO solution is sharper than the regular ENO solution.

5.2.5 Euler equation II: Lax problem

The Lax problem has the following initial conditions:

$$(\rho, u, P) = \begin{cases} (0.445, 0.698, 3.528) & x \leq 0 \\ (0.5, 0, 0.571) & x > 0 \end{cases}$$

with the Dirichlet boundary conditions at $x = 0.5$ and $x = -0.5$. The solution was integrated until $t = 0.13$. Figures 5 and 6 show the solution profiles at the final time $T = 0.13$ with $N = 200$ for $k = 2$ and $k = 3$, respectively. The top left figure shows the global solution and the rest the local solution profile in the areas specified in the top left figure. For $k = 2$, as in the previous example, the RBF-ENO and RBF-WENO-JS solutions are better than the regular ENO and WENO solutions near the non-smooth area. For $k = 3$, the RBF-WENO-JS solution is slightly better than the WENO solution and the RBF-ENO solution is better than the regular ENO solution. Since the RBF-WENO-JS and WENO-JS methods both yield about 5th order accuracy while the RBF-ENO solution is 3rd order or higher but less than 5th order, it is expected that the RBF-WENO-JS or WENO-JS solutions are better than the ENO and RBF-ENO solutions.

5.3 2D Numerical examples

Now we consider the two-dimensional hyperbolic conservation law below

$$u_t(x, y, t) + f_x(u(x, y, t)) + g_y(u(x, y, t)) = 0,$$

with the appropriate initial and boundary conditions where f and g are the flux functions. As in 1D case, the ODE system for the discretized version in the cell $I_{ij} = [x_{i-\frac{1}{2}}, x_{i+\frac{1}{2}}] \times [y_{j-\frac{1}{2}}, y_{j+\frac{1}{2}}]$ is given by

$$\frac{du_{ij}(t)}{dt} = -\frac{1}{\Delta x} [\hat{f}_{i+\frac{1}{2},j} - \hat{f}_{i-\frac{1}{2},j}] - \frac{1}{\Delta y} [\hat{g}_{i,j+\frac{1}{2}} - \hat{g}_{i,j-\frac{1}{2}}], \quad (30)$$

where $u_{ij}(t)$ is the numerical approximation to $u(x_i, y_j, t)$ and \hat{f} and \hat{g} are the numerical fluxes for the flux functions f and g , respectively. Notice that unlike the finite volume method, the finite difference method does not involve any quadrature points for the numerical integration of the flux functions. With the finite volume non-polynomial ENO/WENO methods for 2D problems, the accuracy of the local reconstruction can be enhanced at certain quadrature points. But since there is no quadrature point involved, the finite difference RBF-WENO-JS method maintains the same order of convergence although the accuracy of the RBF-WENO-JS method is enhanced.

For the 2D numerical experiments, we consider the double Mach reflection problem described in [15] with the domain $(x, y) \in [0, 4] \times [0, 1]$. The simulation is run until the final time $T = 0.2$. At $T = 0.2$, shocks form near the right edge shown as an almost straight line in the density contour in the following figures. Figures 7 and 9 show the density contours with various methods. The left column of figures shows the density contours with the regular ENO/WENO methods and the right column with the RBF-ENO/WENO-JS methods. These contours look similar with slight differences. For a detailed comparison, Figs. 8 and 10 show a slice image of Figs. 7 and 9 at $y = 0.5$. We zoom in different regions for the case of $N = 160$ and $M = 40$ (Fig. 8) and $N = 320$ and $M = 80$ (Fig. 10) to compare all the methods. Here N and M denote the total number of grids in x and y directions, respectively. With $k = 2$, we can see that the RBF-ENO solutions are comparable or even better than the regular WENO solutions. This is because when the RBF-ENO and the regular WENO solutions are of the same order, the RBF-ENO solution is sharper and less dissipative. The RBF-WENO-JS solution is also slightly better and sharper than the regular WENO-JS solution. With $k = 3$, the regular WENO solution is better than the RBF-ENO solution since the accuracy of the RBF-ENO method is lower than the regular WENO method. However, the RBF-ENO solution is still sharper than the regular ENO solution and has a similar shape to the WENO solution. We also observe that the RBF-WENO-JS method performs best among all those methods.

6 Conclusion

In this paper, we presented the finite difference RBF-ENO/WENO methods, a direct extension of the non-polynomial ENO/WENO finite volume methods proposed in [4]. The RBF-ENO/WENO finite difference method seeks the reconstruction using the RBF interpolation which involves the free shape parameter. By optimizing the shape parameter, the finite difference RBF-ENO/WENO reconstruction becomes more accurate than the regular ENO/WENO reconstruction for smooth problems and yields sharper solution profiles near the jump discontinuity. The finite difference RBF-ENO reconstruction is sought in terms of the flux function. Accordingly the optimization of the shape parameter of the RBFs is found based on the flux functions on the grid points within the given stencil. Unlike the finite volume RBF-ENO/WENO method, the finite difference RBF-ENO/WENO method does not involve any integral approximation. Thus the order of convergence is fully determined by the size of stencil for 2D problems. Numerical examples both in 1D and 2D show that the finite difference RBF-ENO and RBF-WENO-JS methods yield more accurate results than the regular ENO and WENO-JS methods. Also the solutions by the RBF-ENO and RBF-WENO-JS methods near the discontinuities are sharper than the solutions by the regular ENO/WENO method.

In our current work, we implemented the RBF reconstruction in the regular ENO and WENO methods based on the original WENO reconstruction by Jiang and Shu [9]. As mentioned in the paper, we will investigate the RBF reconstruction with other ENO/WENO variations in our future research such as the WENO-Z method [2]. We were interested in improving local accuracy, but it would be an interesting research to investigate how the local adaption of the shape parameter can be utilized with the meshless properties of RBFs on the unstructured grid. Furthermore, we will also investigate the RBF-ENO/WENO

method for higher values of k than $k = 3$ with multiple shape parameters defined in the RBF basis used for the reconstruction.

Acknowledgments: The authors thank W.-S. Don for his useful communication.

References

- [1] T. ABOIYAR, E. H. GEORGOULIS, A. ISKE, Adaptive ADER methods using kernel-based polyharmonic spline WENO reconstruction, *SIAM J. Sci. Comput.* 32 (6) (2010) pp. 3251–3277.
- [2] R. BORGES, M. CARMONA, B. COSTA, W.S. DON, An improved WENO scheme for hyperbolic conservation laws, *J. Comput. Phys.* 227 (2008) pp. 3191–3211.
- [3] M. D. BUHMAN, Radial basis functions – Theory & Implementations, Cambridge University Press, Cambridge, 2003.
- [4] J. GUO AND J.-H. JUNG, Non-polynomial ENO and WENO finite volume methods for hyperbolic conservation laws, submitted, 2015.
- [5] Y. HA, C. H. KIM, Y. J. LEE, AND J. YOON, An improved weighted essentially non-oscillatory scheme with a new smoothness indicator, *J. Comput. Phys.* 232 (1) (2013), pp. 68–86.
- [6] A. HARTEN, B. ENGQUIST, S. OSHER AND S. R. CHAKRAVARTHY, Uniformly High Order Accurate Essentially Non-Oscillatory Schemes III, *J. Comput. Phys.* 71 (1987) pp. 231–303.
- [7] A. K. HENRICK, T. D. ASLAM, J. M. POWERS, Mapped weighted-essentially-non-oscillatory schemes: achieving optimal order near critical points, *J. Comput. Phys.* 207 (2005) pp. 542–567.
- [8] J. HESTHAVEN, S. GOTTLIEB AND D. GOTTLIEB, Spectral methods for time dependent problems, Cambridge UP, 2007.
- [9] G.-S. JIANG AND C.-W. SHU, Efficient Implementation of weighted ENO schemes, *J. Comput. Phys.* 126 (1996), pp. 202–228.
- [10] E. LARSSON AND B. FORNBERG, Theoretical and computational aspects of multivariate interpolation with increasingly flat radial basis functions, *Comput. Math. Appl.* 49 (2005), pp. 103–130.
- [11] Y. LEE, J. YOON AND C. MICCHELLI, On convergence of flat multivariate interpolation by translation kernels with finite smoothness, *Constructive Approximation*, to appear, 2014.
- [12] C.-W. SHU, Essentially non-oscillatory and weighted essentially non-oscillatory schemes for hyperbolic conservation laws, “Advanced Numerical Approximation of Nonlinear Hyperbolic Equations” (Lecture notes in Mathematics 1697), A. Quarteroni (Ed.), Springer-Verlag, 1998.
- [13] C.-W. SHU, High Order Weighted Essentially Nonoscillatory Schemes for Convection Dominated Problems, *SIAM Rev.* 51(1) (2009), pp. 82–126.
- [14] C.-W. SHU AND S. OSHER, Efficient implementation of essentially non-oscillatory shock-capturing schemes, *J. Comput. Phys.* 77 (1988), pp. 439–471.
- [15] P. WOODWARD AND P. COLELLA, The numerical simulation of two-dimensional fluid flow with strong shocks, *J. of Comput. Phys.* 54 (1984), pp. 115–173.

Table 5: L_1, L_2 and L_∞ errors for the advection equation (24) with continuous initial condition (25). $T = 0.5$. $k = 2$.

Method	N	L_1 error	L_1 order	L_2 error	L_2 order	L_∞ error	L_∞ order
ENO $k = 2$	10	1.11E-1	–	1.40E-1	–	2.22E-1	–
	20	4.61E-2	1.2689	5.32E-2	1.3994	9.43E-2	1.2375
	40	1.37E-2	1.7458	1.79E-2	1.5749	4.03E-2	1.2236
	80	3.81E-3	1.8530	5.69E-3	1.6492	1.68E-2	1.2614
	160	1.02E-3	1.8901	1.80E-3	1.6599	6.91E-3	1.2849
	320	2.71E-4	1.9224	5.69E-4	1.6613	2.81E-3	1.2964
RBF-ENO $k = 2$	10	1.79E-2	–	2.35E-2	–	4.24E-2	–
	20	2.48E-3	2.8540	2.65E-3	3.1473	3.62E-3	3.5495
	40	3.17E-4	2.9673	3.43E-4	2.9488	4.79E-4	2.9207
	80	4.05E-5	2.9704	4.42E-5	2.9592	6.22E-5	2.9434
	160	5.17E-6	2.9702	5.60E-6	2.9810	7.97E-6	2.9652
	320	6.51E-7	2.9897	7.05E-7	2.9892	1.00E-6	2.9894
WENO-JS $k = 2$	10	9.13E-2	–	1.10E-1	–	1.74E-1	–
	20	2.92E-2	1.6453	3.26E-2	1.7588	5.51E-2	1.6547
	40	4.81E-3	2.5998	6.33E-3	2.3645	1.38E-2	2.0037
	80	6.42E-4	2.9066	9.43E-4	2.7470	2.61E-3	2.3979
	160	7.79E-5	3.0440	1.23E-4	2.9427	3.96E-4	2.7183
	320	9.54E-6	3.0291	1.53E-5	3.0035	5.25E-5	2.9181
RBF-WENO-JS $k = 2$	10	1.88E-2	–	2.38E-2	–	4.06E-2	–
	20	2.60E-3	2.8561	2.73E-3	3.1235	4.13E-3	3.2995
	40	3.25E-4	2.9969	3.57E-4	2.9367	5.36E-4	2.9442
	80	4.05E-5	3.0064	4.50E-5	2.9871	6.75E-5	2.9896
	160	5.09E-6	2.9910	5.63E-6	2.9983	8.32E-6	3.0199
	320	6.40E-7	2.9927	7.04E-7	3.0000	1.00E-6	3.0539

Table 6: L_1, L_2 and L_∞ errors for the advection equation (24) with continuous initial condition (25). $T = 0.5$. $k = 3$.

Method	N	L_1 error	L_1 order	L_2 error	L_2 order	L_∞ error	L_∞ order
ENO $k = 3$	10	2.32E-2	–	2.54E-2	–	3.65E-2	–
	20	2.79E-3	3.0570	3.02E-3	3.0727	4.47E-3	3.0314
	40	3.36E-4	3.0519	3.69E-4	3.0360	5.47E-4	3.0293
	80	4.12E-5	3.0284	4.55E-5	3.0189	6.76E-5	3.0167
	160	5.10E-6	3.0146	5.65E-6	3.0099	8.53E-6	2.9878
	320	6.34E-7	3.0074	7.03E-7	3.0051	1.06E-6	3.0082
RBF-ENO $k = 3$	10	1.89E-2	–	2.22E-2	–	3.45E-2	–
	20	2.15E-3	3.1332	2.59E-3	3.1022	4.47E-3	2.9462
	40	1.51E-4	3.8321	2.18E-4	3.5731	5.14E-4	3.1218
	80	8.81E-6	4.1023	1.57E-5	3.7941	5.10E-5	3.3319
	160	4.83E-7	4.1891	1.06E-6	3.8854	4.60E-6	3.4706
	320	2.78E-8	4.1205	7.30E-8	3.8618	4.25E-7	3.4372
WENO-JS $k = 3$	10	9.74E-3	–	1.13E-2	–	1.63E-2	–
	20	4.01E-4	4.6032	4.63E-4	4.6147	7.82E-4	4.3822
	40	1.17E-5	5.0966	1.37E-5	5.0804	2.45E-5	4.9965
	80	3.55E-7	5.0452	4.10E-7	5.0617	7.55E-7	5.0196
	160	1.12E-8	4.9825	1.27E-8	5.0100	2.33E-8	5.0180
	320	3.80E-10	4.8849	4.25E-10	4.9022	6.94E-10	5.0692
RBF-WENO-JS $k = 3$	10	6.53E-3	–	7.90E-3	–	1.16E-2	–
	20	1.22E-5	5.7476	1.50E-4	5.7155	2.72E-4	5.4183
	40	2.58E-6	5.5559	3.24E-6	5.5380	8.04E-6	5.0796
	80	7.51E-8	5.1050	8.72E-8	5.2129	2.17E-7	5.2082
	160	2.35E-9	4.9964	2.63E-9	5.0497	5.58E-9	5.2833
	320	7.39E-11	4.9920	8.22E-11	5.0014	1.46E-10	5.2581

Table 7: L_1, L_2 and L_∞ errors for the Burgers' equation (27) with continuous initial condition (28). $T = 0.2$. $k = 2$.

Method	N	L_1 error	L_1 order	L_2 error	L_2 order	L_∞ error	L_∞ order
ENO $k = 2$	10	5.38E-2	–	8.24E-2	–	1.71E-1	–
	20	1.98E-2	1.4464	2.81E-2	1.5521	5.74E-2	1.5716
	40	5.40E-3	1.8715	8.28E-3	1.7628	2.12E-2	1.4355
	80	1.31E-3	2.0396	2.52E-3	1.7183	8.85E-3	1.2619
	160	3.85E-4	1.7690	8.13E-3	1.6309	3.64E-3	1.2816
	320	1.07E-4	1.8475	2.59E-4	1.6519	1.49E-3	1.2928
RBF-ENO $k = 2$	10	4.13E-2	–	4.52E-2	–	1.16E-1	–
	20	7.41E-3	2.4795	1.53E-2	1.5817	4.63E-2	1.3254
	40	1.08E-3	2.7836	3.01E-3	2.3418	1.18E-2	1.9714
	80	1.38E-4	2.9656	4.22E-4	2.8362	1.81E-3	2.7073
	160	1.55E-5	3.1548	4.89E-5	3.1107	2.40E-4	2.9135
	320	1.75E-6	3.1415	5.54E-6	3.1396	2.67E-5	3.1669
WENO-JS $k = 2$	10	4.61E-2	–	7.23E-2	–	1.55E-1	–
	20	1.27E-2	1.8592	1.96E-2	1.8792	4.43E-2	1.8056
	40	1.97E-3	2.6901	3.13E-3	2.6493	8.18E-3	2.4392
	80	2.99E-4	2.7199	5.22E-4	2.5851	1.40E-3	2.5473
	160	4.32E-5	2.7893	7.89E-5	2.7252	2.49E-4	2.4893
	320	5.75E-6	2.9100	1.07E-5	2.8769	3.68E-5	2.7572
RBF-WENO-JS $k = 2$	10	2.50E-2	–	3.69E-2	–	7.02E-2	–
	20	6.64E-3	1.9158	1.57E-2	1.2310	4.88E-2	0.5227
	40	1.05E-3	2.6662	3.06E-3	2.3610	1.28E-2	1.9376
	80	1.30E-4	3.0062	4.03E-4	2.9230	1.70E-3	2.9098
	160	1.50E-5	3.1181	4.62E-5	3.1254	2.15E-4	2.9772
	320	1.73E-6	3.1128	5.29E-6	3.1286	2.45E-5	3.1374

Table 8: L_1, L_2 and L_∞ errors for the Burgers' equation (27) with continuous initial condition (28). $T = 0.2$. $k = 3$.

Method	N	L_1 error	L_1 order	L_2 error	L_2 order	L_∞ error	L_∞ order
ENO $k = 3$	10	2.00E-2	–	3.63E-2	–	7.95E-2	–
	20	4.89E-3	2.0328	7.77E-3	2.2243	1.57E-2	2.3449
	40	8.68E-4	2.4953	1.50E-3	2.3751	4.93E-3	1.6676
	80	1.25E-4	2.7961	2.21E-4	2.7622	6.38E-4	2.9499
	160	1.84E-5	2.7675	3.44E-5	2.6816	1.32E-4	2.2697
	320	2.84E-6	2.6918	5.68E-6	2.5991	2.84E-5	2.2184
RBF-ENO $k = 3$	10	1.87E-2	–	3.48E-2	–	7.70E-2	–
	20	4.05E-3	2.2024	6.22E-3	2.4851	1.44E-2	2.4187
	40	6.21E-4	2.7069	1.17E-3	2.4052	3.55E-3	2.0213
	80	1.22E-4	2.3453	3.00E-4	1.9658	1.53E-3	1.2130
	160	1.03E-5	3.5705	3.00E-5	3.3226	1.91E-4	3.0040
	320	8.23E-7	3.6436	2.76E-6	3.4444	2.09E-5	3.1898
WENO-JS $k = 3$	10	1.28E-2	–	2.21E-2	–	4.75E-2	–
	20	2.67E-3	2.2595	4.97E-3	2.1570	1.49E-2	1.6760
	40	2.83E-4	3.2361	8.51E-4	2.5439	3.75E-3	1.9854
	80	1.53E-5	4.2131	5.48E-5	3.9567	3.20E-4	3.5528
	160	6.08E-7	4.6500	1.93E-6	4.8298	1.15E-5	4.7908
	320	1.80E-8	5.0792	5.56E-8	5.1168	3.35E-7	5.1071
RBF-WENO-JS $k = 3$	10	1.06E-2	–	1.87E-2	–	4.09E-2	–
	20	1.71E-3	2.6282	2.65E-3	2.8170	7.09E-3	2.5284
	40	2.53E-4	2.7592	6.44E-4	2.0428	2.62E-3	1.4336
	80	1.40E-5	4.1748	4.82E-5	3.7417	2.77E-4	3.2434
	160	4.93E-7	4.8277	1.67E-6	4.8488	1.00E-5	4.7930
	320	1.46E-8	5.0755	4.83E-8	5.1130	2.88E-7	5.1170

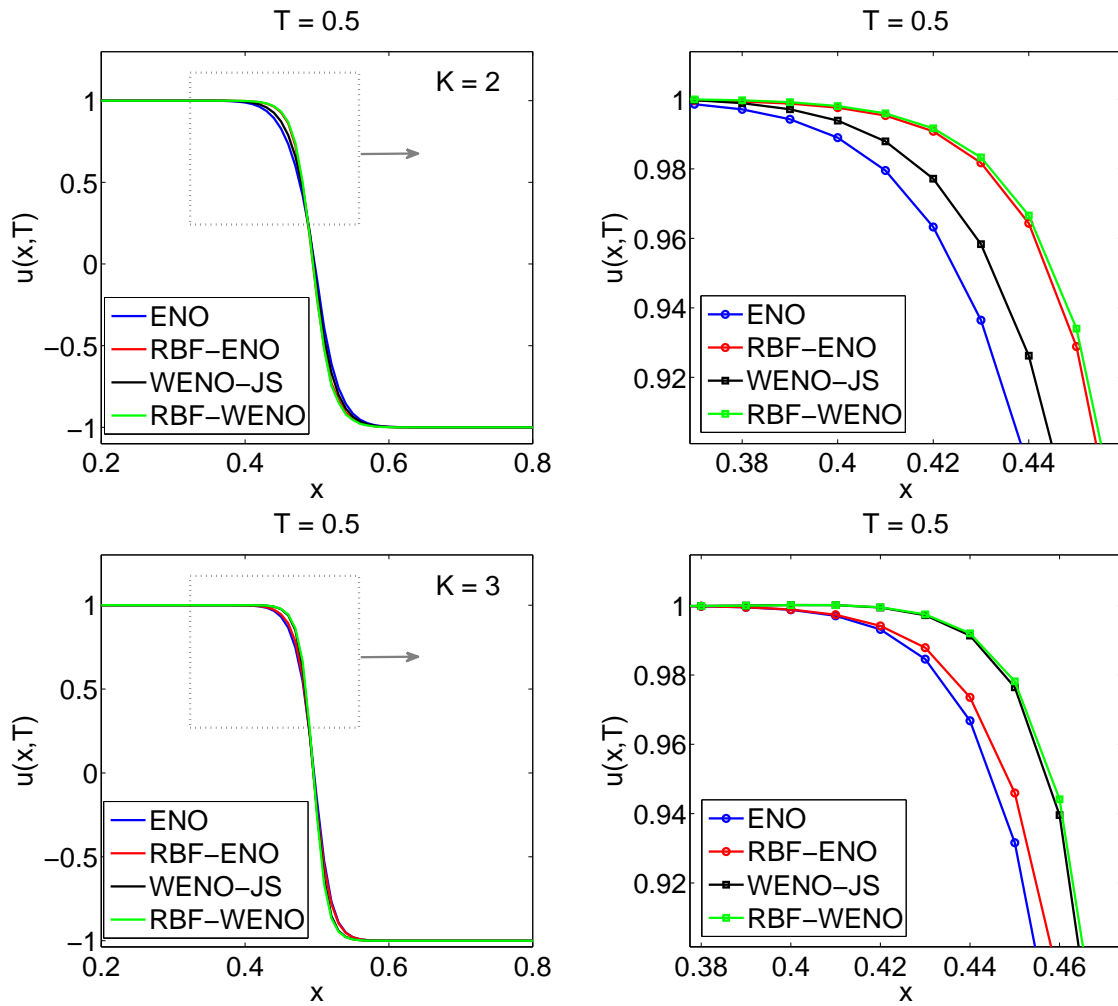
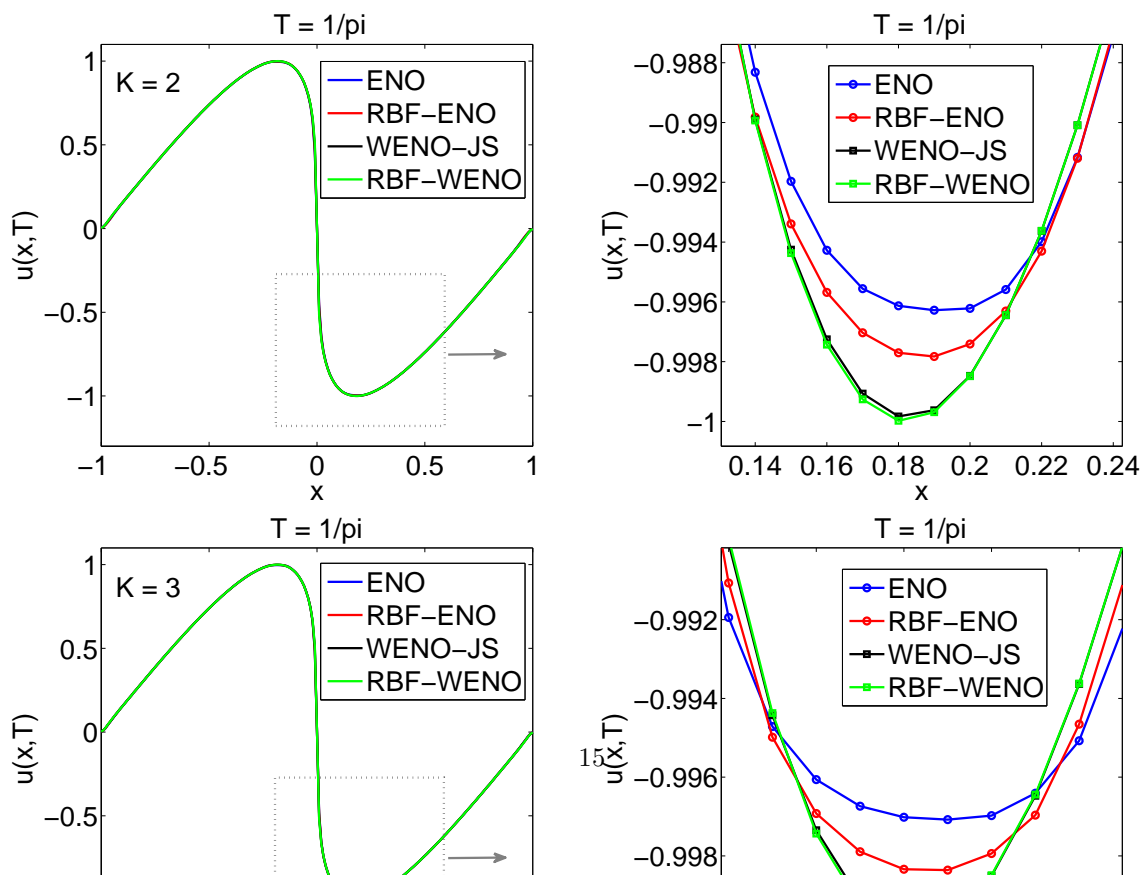


Figure 1: Solutions to advection equation (24) with discontinuous initial condition (26). $T = 0.5$. $k = 2$ (top) and $k = 3$ (bottom). $N = 200$.



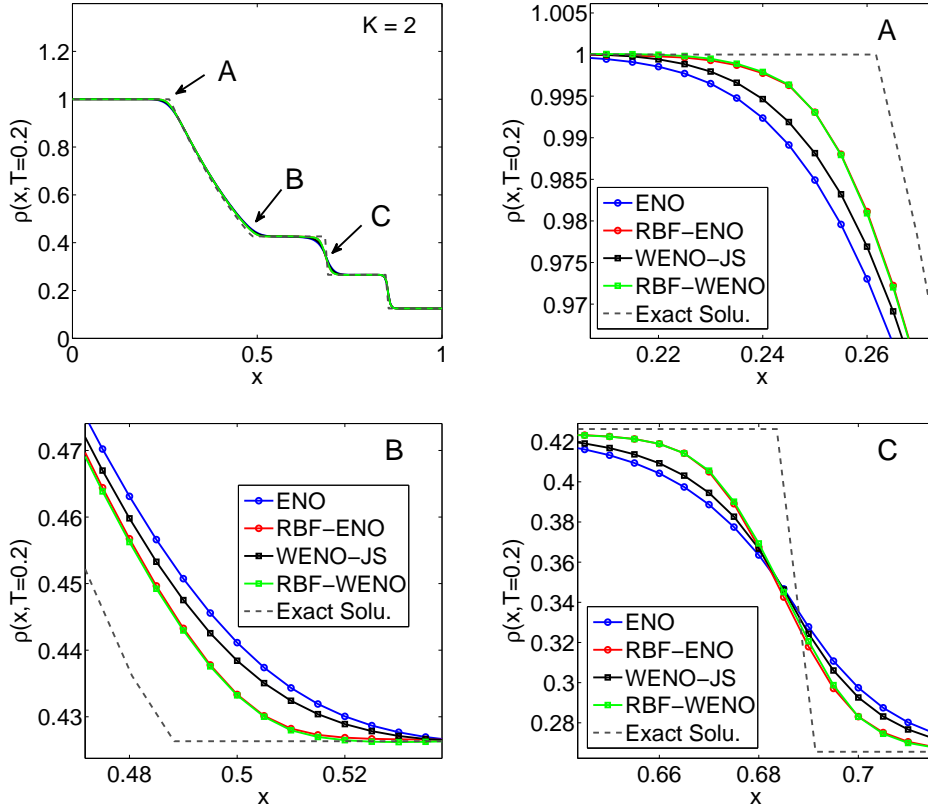


Figure 3: Density profiles for Sod problem. $T = 0.2$. $N = 400$. $k = 2$. The dashed line is the exact solution.

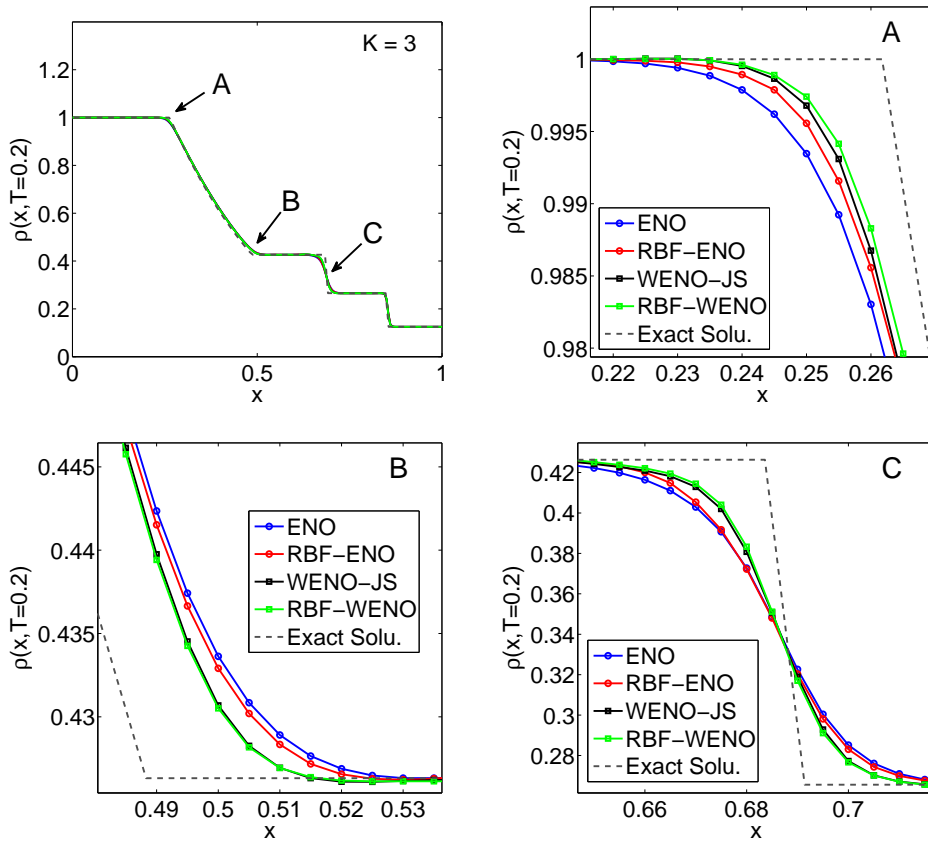


Figure 4: Density profiles for Sod problem. $T = 0.2$. $N = 600$. $k = 3$. The dashed line is the exact solution.

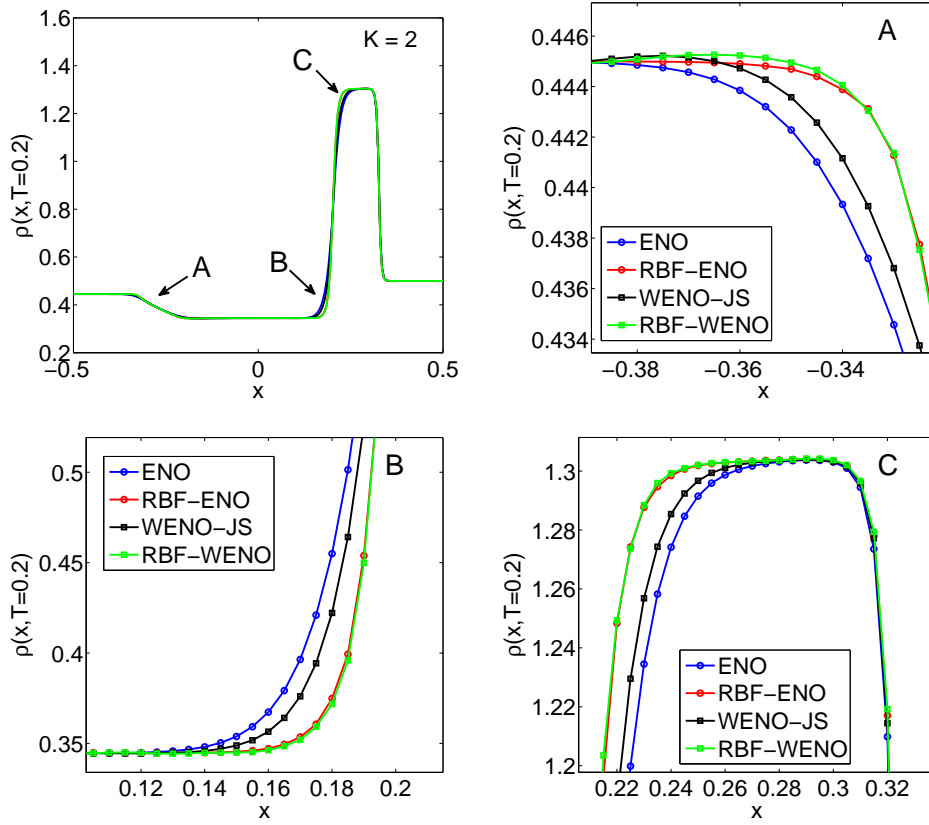


Figure 5: Density profiles for Lax problem. $T = 0.13$. $N = 200$. $k = 2$.

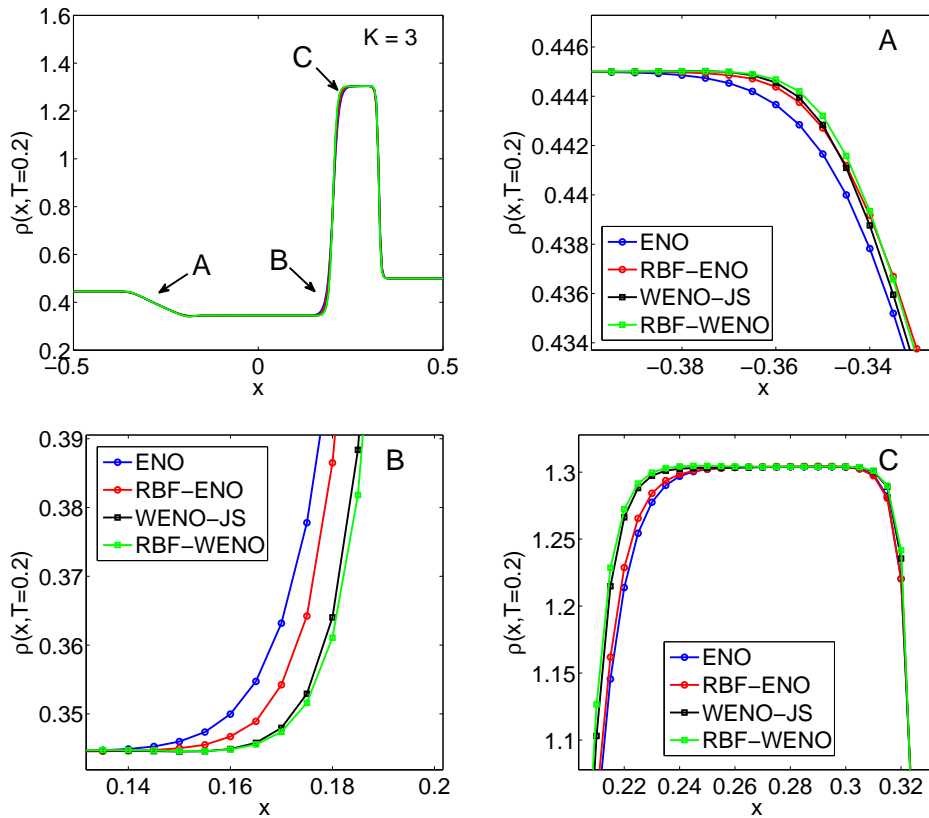


Figure 6: Density profiles for Lax problem. $T = 0.13$. $N = 200$. $k = 3$.

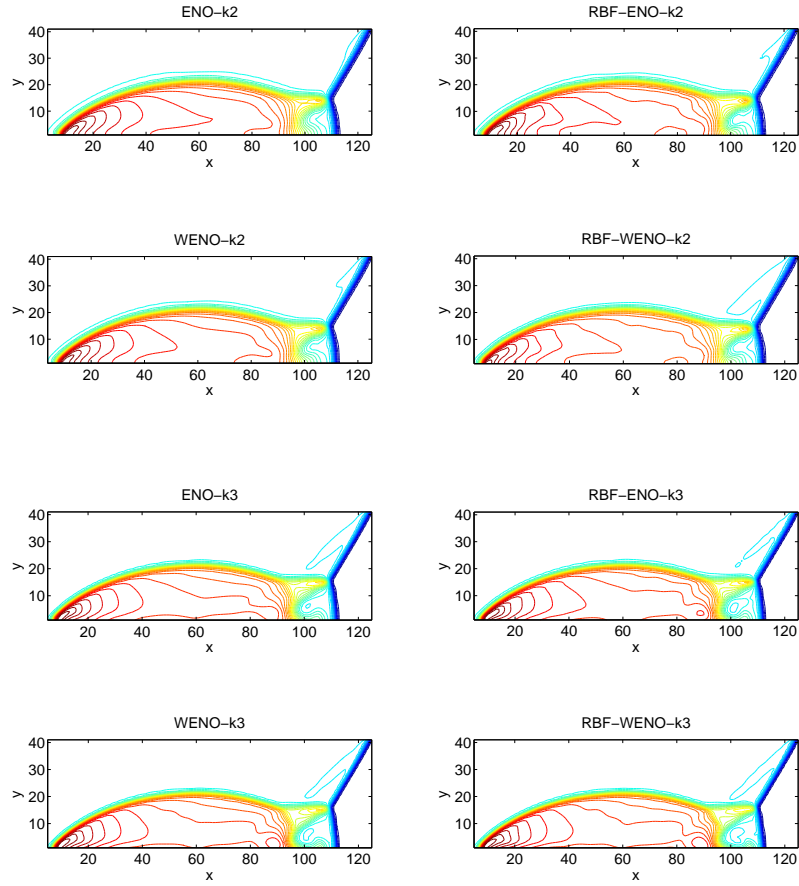


Figure 7: Density contours for the Double Mach Reflection problem. $T = 0.2$. $N = 160$. $M = 40$.

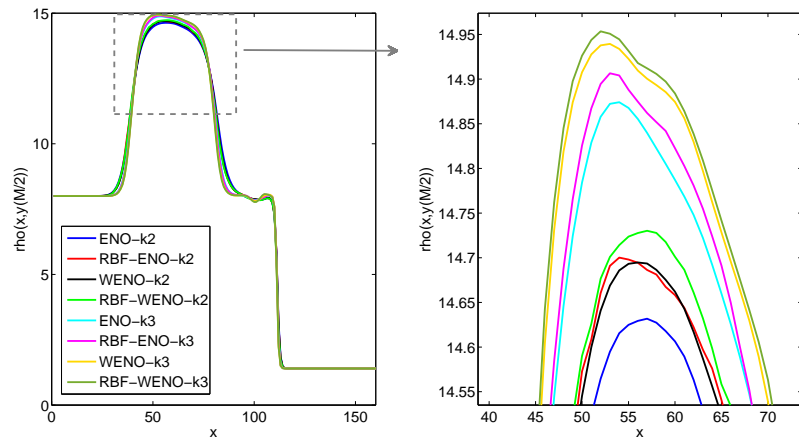


Figure 8: Density profiles at $y = 0.5$ for the Double Mach Reflection problem. $T = 0.2$. $N = 160$. $M = 40$.

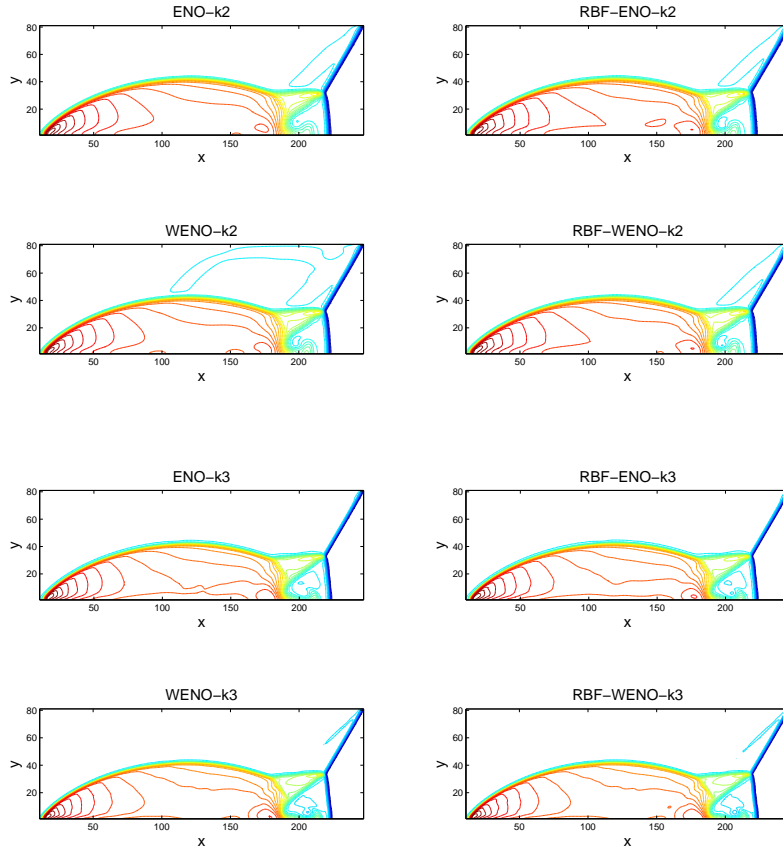


Figure 9: Density contours for the Double Mach Reflection problem. $T = 0.2$. $N = 320$. $M = 80$.

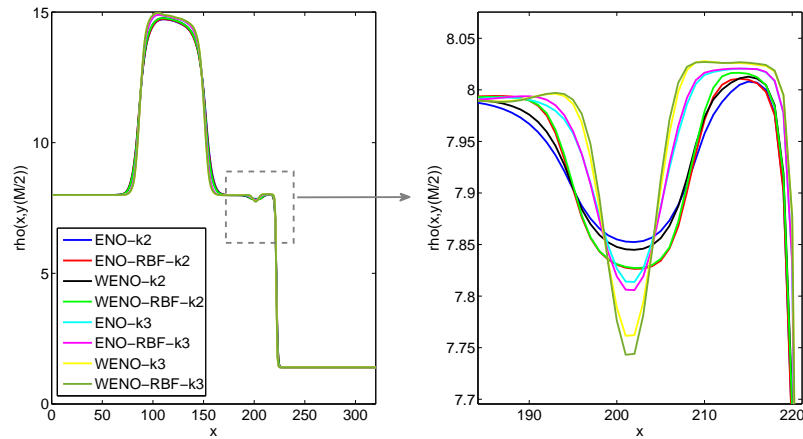


Figure 10: Density profiles at $y = 0.5$ for the Double Mach Reflection problem. $T = 0.2$. $N = 320$. $M = 80$.